# Quantitative assessment of the interfacial roughness in multi-layered materials using image analysis: Application to oxidation in ceramic-based materials

Sabine Le Roux, Frédéric Deschaux-Beaume, Thierry Cutard, Philippe Lours

# Quantitative assessment of the interfacial roughness in multi-layered materials using image analysis: Application to oxidation in ceramic-based materials

S. Le Roux [1*], F. Deschaux-Beaume[2], T. Cutard[1], P. Lours[1]

*1 Université de Toulouse, Mines Albi, INSA, ISAE, UPS, ICA (Institut Clément Ader); Campus Jarlard, F-81013 Albi cedex 09, France*
*2 Laboratoire de Mécanique et Génie Civil (LMGC), Université de Montpellier, CNRS, Montpellier, France*

**Abstract**

A method is developed to characterize interfacial roughness of layered materials. A series of contiguous images is acquired with a Scanning Electron Microscope on polished cross-sections. Using image analysis algorithms based on mathematical morphology operations, interface profiles are extracted and mathematically processed to calculate standard surface roughness parameters. In addition, morphological criteria describing the interface tortuosity are determined, such as the "normalized rumpling index" (based on the profile developed length) and the "barbule density" that quantifies the protrusions of the layer (using the skeletonization function). The validity and accuracy of the method is evaluated by comparison with measurements performed by the conventional surface metrology techniques. This method is used to study internal oxidation of two ceramic-based materials ($Si_3N_4$–TiN composite/thermal barrier coatings) upon thermal aging. In both cases, a link is established between the roughening of the oxide layer interface and a decrease in the mechanical strength of the multi-layered material.

*Keywords:* Interfacial roughness; SEM image analysis; Thermal aging; Oxidation; Thermal barrier coating systems

## 1. Introduction

As a material is subject to a thermal aging or thermo-mechanical loading, an oxide layer generally grows at the surface, whose nature, thickness and morphology depend on the composition of the substrate material, the temperature and exposure time, and the applied or residual stresses. It is well known that the presence of a corrosion layer locally alters the intrinsic properties of the material, often impacting its mechanical strength.[1–6] To prevent such premature damage of the material, it can be useful to deposit a protective coating on its surface (by CVD, PVD, plasma spraying, laser cladding or sputtering, sol–gel process, etc.). It was largely demonstrated that whatever the coating nature and the deposition process, the initial roughness of the substrate strongly influences the bonding mechanisms and the adhesion strength of the coating,[7–11] by favoring the mechanical anchoring on the substrate. On the other hand, both oxide and protective layers create an internal interface with the base material, that undergoes chemical or morphological changes during the oxidation/coating process, or under the effect of thermal or thermo-mechanical loading. The interfacial "roughness" – which may vary depending on the oxidation/coating conditions – probably affects the layer adhesion to the substrate, and therefore the mechanical behavior of the material when submitted to a strong thermal gradient, a mechanical loading or wear. In the particular case of thermal barrier coating (TBC) systems or compositionally graded materials, several interfaces can be observed.[12,13] Several authors[12–15] have reported that a disrupted interface of the aluminide bond coat, which constitutes a site of high stress concentration, can promote failure mechanisms by large-scale spallation or delamination of the coating during cyclic exposure at high temperature. Therefore, it can be relevant to characterize the morphology of the weak interface beside other microstructural properties (such

* Corresponding author. Tel.: +33 563493057; fax: +33 563493099.
*E-mail address:* leroux@mines-albi.fr (S. Le Roux).

as the phase transformations, the coating thickness, etc.), in order to better understand and predict the durability of such multi-layered materials (and especially the coating adherence) under thermal or mechanical stress.[16–19]

Quantifying surface roughness of an external layer is easy and straightforward, using conventional measuring devices such as mechanical probe instruments (contact stylus profiler, Atomic Force Microscope) or non-contact optical sensors (white-ligth or laser extended field confocal microscope, scanning interferometer, optical scatterometer).[20] Different resolutions and measurement ranges can be achieved depending on the measuring technique, and must be selected considering the nature of the material and the required accuracy.[21,22] Such devices are however inappropriate to characterize the morphology of sub-layers, since they do not allow access to the internal interfaces. In this case, a microstructural analysis is required, based on metallographic observations of cross-sections of the multi-material. The layer interface can be highlighted using an optical or scanning electron microscope (SEM), depending on the investigated scale of observation and the nature of the contrast between the different constituents of the layered material. However, these observations remain most often qualitative, even if some mathematical tools (like the fractal dimension $D$ established by Mandelbrot[23,24] or the correlation function of the Fourier spectrum[25]) can help to characterize the complex geometry of fracture surfaces,[26–28] or to evaluate the adhesive strength of coatings.[10] Tolpygo et al.[14] employed a non-destructive technique, based on the photostimulated luminescence spectroscopy, to monitor the damage and morphological changes of a layer interface during thermal aging or cycling. But even if the frequency shift observed on luminescence spectra provides interesting information, it remains insufficient alone to characterize and interpret unambiguously the layer damage. Using image analysis, the same authors[29] also quantified the top surface roughness and undulation of bond coats through quantitative parameters such as the *RMS* and the "tortuosity ratio" (corresponding to the lineal roughness). However, the detection of an internal interface is usually more complex, due to the presence of several layers or phase transformations in the micrographies.

This paper proposes a methodology for quantitative morphometric analysis of interface(s) in layered materials, based on image analysis of SEM micrographs in cross-section. An algorithm is developed using mathematical morphology operations[30] in order to extract the interface profile, which is mathematically processed to separate roughness from waviness. Various morphological criteria and standard surface parameters are then calculated to evaluate the roughness and the corrugation of the profile. The validation of this method is provided by comparison with conventional measurements performed with a stylus profiler and a white light extended field confocal microscope. A first application, aiming to investigate the effect of oxidation on the mechanical behavior at high temperature of a non-oxide ceramic composite, is presented. The second application deals with the evolution of the oxide ratcheting and interface rumpling of EB-PVD TBC systems as a function of thermal aging conditions. Data resulting from these investigations can be used beneficially to implement mechanistics models for achieving a complete analysis of the local high temperature mechanical behavior of multi-layered materials. In such a case, this would require also to include microstructural features (size and crystal orientation of grains, voids and porosities, etc.) which are not deliberately considered here.

## 2. Experimental methodology

### 2.1. Sample preparation and SEM observation

In order to observe the oxide layer or the coating in cross section, the material is cut in the transverse direction and coated in a thick resin. Polished sections are prepared following classical metallographic procedures. Then, the sample is observed in SEM using a back-scattered electron (BSE) detector. This allows to distinguish the various phases present in the material, which appear in different gray levels according to the atomic number of the chemical constituents. The parallelism between the sample surface and the horizontal border of the image is adjusted at a low magnification. Then, a higher magnification, which may vary depending on the layer thickness and morphology, is selected in order to highlight both the layer and the substrate/layer interface with sufficient accuracy (Fig. 1). A spatial resolution $r \leq 1\ \mu m$ (i.e. near or better than lateral resolution commonly achieved with a conventional profiler) is required. This spatial resolution also reflects the height resolution (considering the amplitude of the profile along the $z$-axis), since the pixels of the image are square-shaped. A series of contiguous fields is recorded in order to represent the layer profile on an equivalent length of 4.8 mm (corresponding to the scanning length $l_t$ recommended by the surface metrology standard).[31] The total number $N$ of images to acquire depends on the magnification factor, which must be selected in order to have a high enough spatial resolution. The size of the image (i.e. its number of pixels) can be an interesting adjustment parameter to reduce the magnification, but must however not be too large in order to optimize the processing time (as images with higher spatial resolution are longer to process).

### 2.2. Image analysis

Using the image analysis software Aphelion®, an algorithm is developed in order to extract the profile of the investigated surface (or interface) on each image-field of the series. In the example of Fig. 2, the detection of the top oxide layer profile consists in five steps. First, the contrast of the initial SEM image (Fig. 2a) is enhanced by applying a square function using look-up table (Fig. 2b). Then, the oxide layer is detected by gray level thresholding, based on the difference in phase contrast in the BSE image (Fig. 2c). The resulting binary image may contain noise (here some holes due to black porosities in the ceramic matrix) which must be "cleaned" using mathematical morphology operators, such as closing and hole filling operators (Fig. 2d). The next step aims to extract the surface or interface profile by applying an erosion of size 1 to image (d) (Fig. 2e), then a logical difference between images (d) and (e) (before and after erosion, respectively). This results in representing the surface profile as a continuous line of one pixel-thick (Fig. 2f).

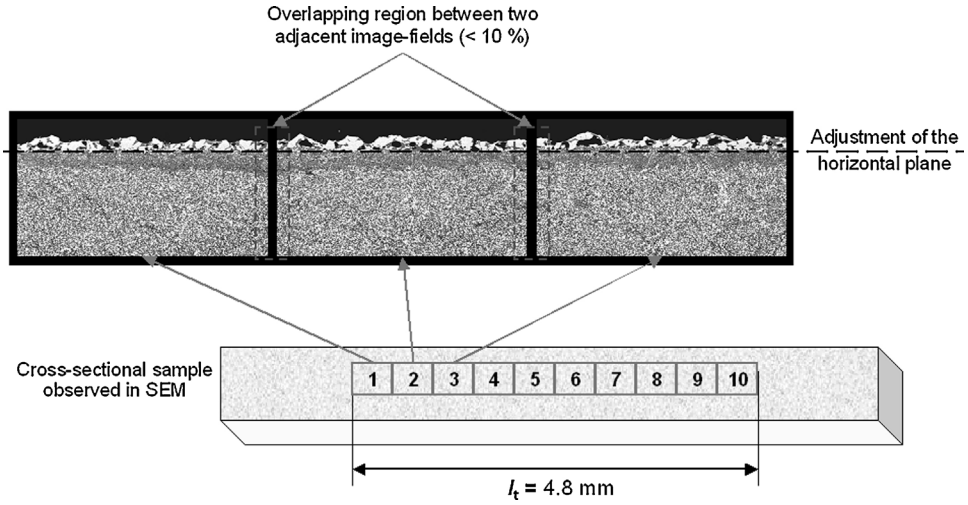


Fig. 1. Procedure for SEM image acquisition: in this example, a series of 10 images is scanned along the layer on a total length ($l_t$) of 4.8 mm (the covering area between two adjacent fields is of about 10%).

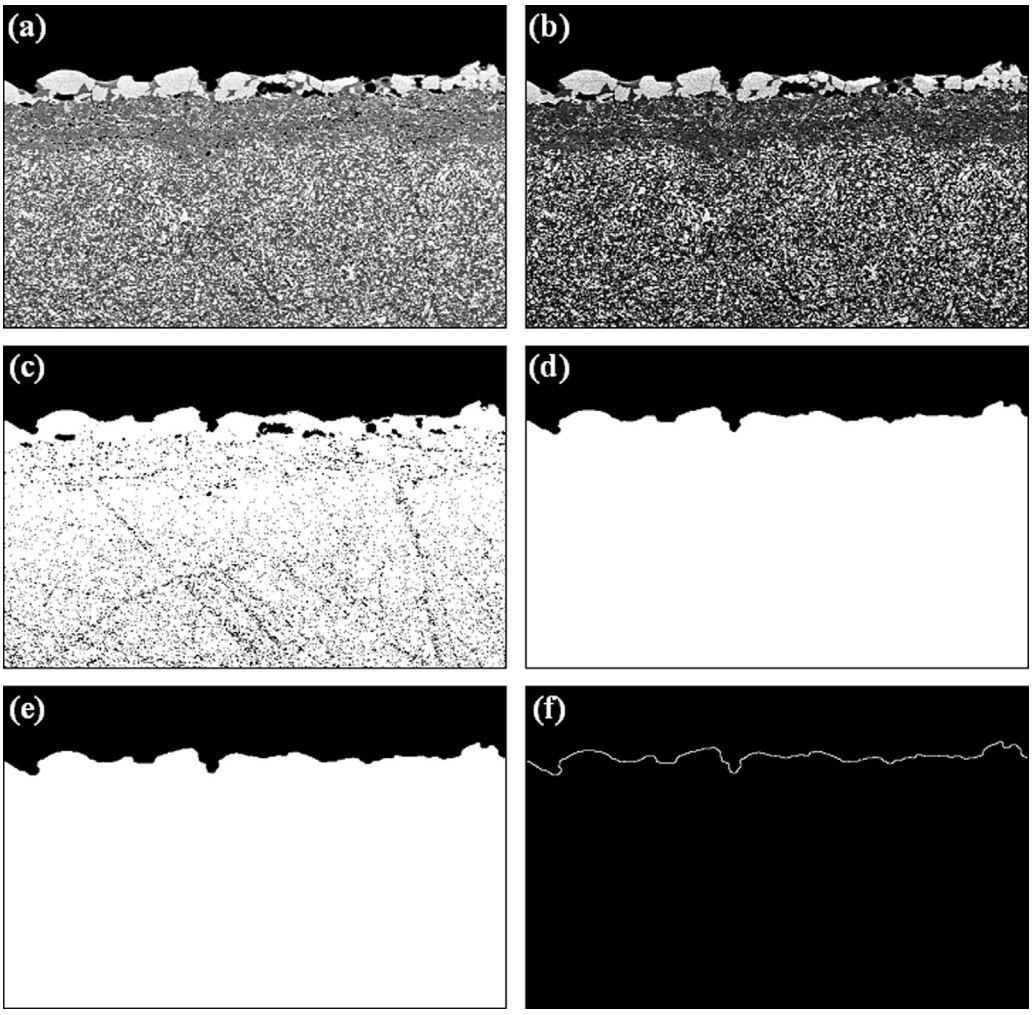


Fig. 2. Image analysis procedure to extract the profile of the top oxide layer thermally grown on a ceramic composite ($Si_3N_4$–TiN): (a) initial SEM image with a magnification of ×1500, showing a phase contrast (BSE detector); (b) contrast enhancement by applying a square LUT; (c) gray-level thresholding; (d) cleaning of the binary image by morphological operations (closing and hole filling of porosities); (e) erosion of size 1, removing one pixel on the contour of the binary object; (f) detection of the profile of the top oxide layer by logical difference of binary images (d) and (e).

Finally, the list of points composing the profiles extracted from each image is saved in an *ASCII* file, as a table of two colums (abcissa $x$ and height $z(x)$, both expressed in pixels).

### 2.3. *Mathematical processing of the profiles*

The ASCII profile files extracted from the $N$ images are processed using the mathematical software Matlab®. The first step consists in editing a single file gathering the data of all profiles, by ensuring the proper matching between the coordinates (abscissa $x$ and height $z$) of the last point $p_f$ of the profile extracted in the image $j$ and those of the first point $p_1$ of the profile extracted in the image $(j+1)$. For instance, each $x(p_i)$ value of the profile $(j+1)$ is corrected by adding $\Delta x$:

$$\Delta x = x(p_f)_j - x(p_1)_{j+1} + 1 \tag{1}$$

The vertical offset along $z$-axis which may exist between two adjacent images must also be corrected, by adding $\Delta z$ to each $z(p_i)$ values of profile $(j+1)$ as follow:

$$\Delta z = z(p_f)_j - z(p_1)_{j+1}. \tag{2}$$

At this stage, the total profile resulting from the assembly of the $N$ profiles consists of a list of $n$ connected points, whose $x$ and $z$ coordinates are still expressed in pixels (Fig. 3a). It is therefore required to calibrate these values in micrometers, by multiplying each column $(x,z)$ of the profile file by the spatial resolution $r$ of the images. The resulting raw profile contains a range of spatial frequencies, from the form (low frequency components of large wavelength), the waviness (medium frequency components) to the actual roughness (high frequency irregularities). Forms errors, and especially the residual tilt of the profile with respect to the horizontal plane, can be removed by using a least-squares regression.[32] This method consists in choosing the values of coefficients $a$ and $b$ to minimize the residue $E$ (sum of square deviations), as expressed by the equations:

$$E = \sum_{i=0}^{n} \varepsilon_i^2 = \sum_{i=0}^{n} (z_i - (ax_i + b))^2, \tag{3}$$

with

$$a = \frac{n\sum_{i=1}^{n} x_i, z_i - \sum_{i=1}^{n} x_i \sum_{i=1}^{n} z_i}{n\sum_{i=1}^{n} {x_i}^2 - \left(\sum_{i=1}^{n} x_i\right)^2} \quad \text{and} \quad b = \frac{\sum_{i=1}^{n} z_i}{n} - a\frac{\sum_{i=1}^{n} x_i}{n}, \tag{4}$$

where $n$ is the total number of points in the profile, $x_i$ is the position of point $i$ along the $x$-axis, and $z_i$ is the height of point $i$ along the $z$-axis.

The primary profile, which results from the subtraction of the least-squares line to the raw profile, contains both waviness and roughness components (Fig. 3b). In order to separate this two ranges of wavelengths, the primary profile is filtered with a low-pass filter, as implemented by the convolution function:

$$m(x) = z \times s(x), \tag{5}$$

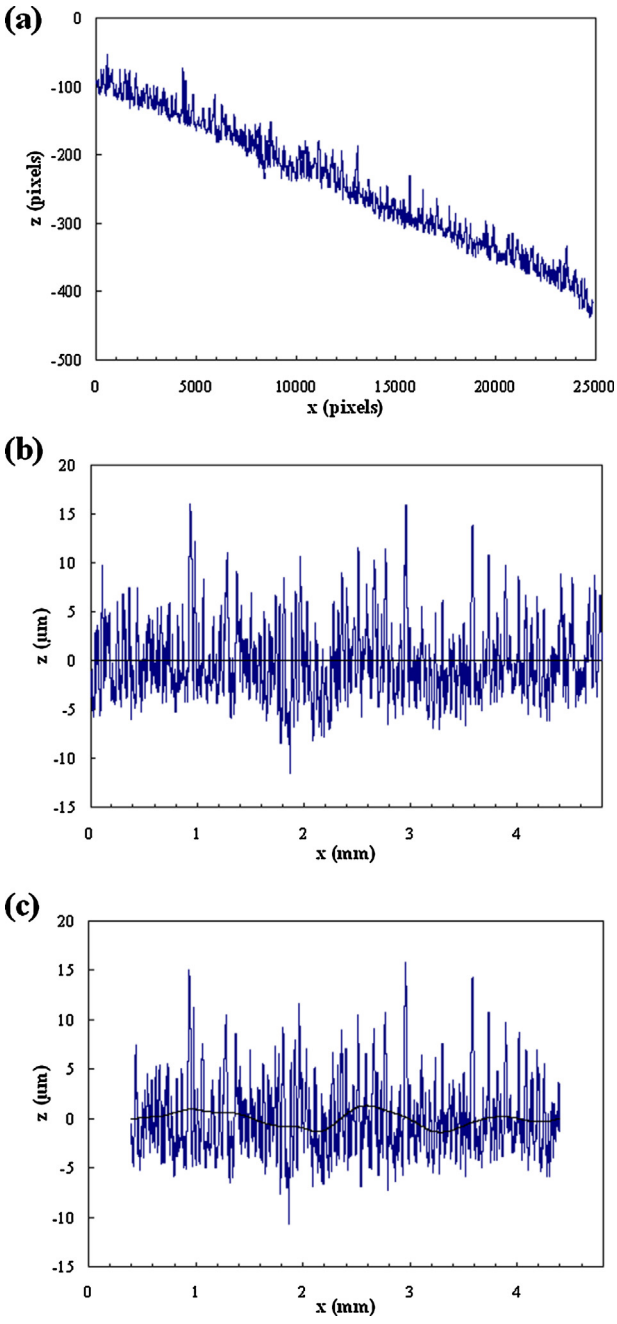


Fig. 3. Mathematical processing of the profiles: (a) total raw profile resulting from the assembly of the profiles extracted from the $N$ contiguous images; (b) calibrated primary profile, leveled by least-squares regression (the sampling length is $l_t = 4.8$ mm); (c) roughness profile (short wave profile components), obtained by subtracting the mean line to the primary profile (the mean line is superimposed to the roughness profile). Note that the evaluation length is reduced to $l_e = 4$ mm.

where $m(x)$ is the output filtered profile, $z(x)$ is the input primary profile, and $s(x)$ is the impulsional response of the filter.

Eq. (5) is applied using a sliding weighted kernel function, which allows to reconstruct the so-called "mean line" $m(x)$ of the profile (corresponding to the reference line used for surface assessment).[33,34] According to the ISO 11562 standard,[35] the

Table 1
Effect of the image magnification and resolution on the calculated value of the fractal parameter $L_d/L_p$.

| Image magnification | Image horizontal length (pixels) | Spatial resolution (μm/pixel) | Profile developed length (pixel) | $L_d/L_p$ |
|---|---|---|---|---|
| ×500 | 818 | 0.124 | 1194 | 1.460 |
| **×750** | **1228** | **0.083** | **1808** | **1.472** |
| ×1000 | 1635 | 0.062 | 2408 | 1.473 |
| ×1250 | 2048 | 0.050 | 3025 | 1.477 |
| | | | Mean value | 1.470 |
| | | | Standard deviation | 0.007 |
| | | | Coef. of variation (%) | 0.510 |

most widely used filter is the Gaussian filter, whose weighting function[34] is given by:

$$s(x) = \frac{1}{\alpha\lambda_c} \exp\left(-\pi\left(\frac{x}{\alpha\lambda_c}\right)^2\right) \quad (6)$$

where $\alpha$ is a constant ($\alpha = 0.4697$), and $\lambda_c$ is the cut-off wavelength.

The ordinate of the mean line at each point of abscissa $x_0$ thus results from the calculation of the weighted average of the profile points located on either side, the ordinate of each point being weighted by a value $s(\delta)$, function of its distance $\delta$ ($=x - x_0$) at the considered point, as described by the equation:

$$m(x_0) = \int_{x_0-\lambda_c}^{x_0+\lambda_c} z(x)s(x_0 - x)dx \quad (7)$$

Finally, the roughness profile $r(x)$, corresponding to short wave profile components (Fig. 3c), is obtained by subtracting the mean line $m(x)$ to the primary profile $z(x)$:

$$r(x) = z(x) - m(x) \quad (8)$$

The influence of the cut-off length on the roughness parameters and the necessity to choose an appropriate value in order to avoid distorsions has been largely emphasized.[20,32,33] In the following applications, a cut-off value of 0.8 mm was selected, as provided by International Standard ISO 11562.[35] As mentioned above, the sampling length ($l_t$) of the profile is 4.8 mm, so as $l_t = 6\lambda_c$. However, the evaluation length ($l_e$) should be reduced to 4 mm ($l_e = 5\lambda_c$), in order to eliminate distorsion effects at the beginning and the end of the filtered profile by removing the first half and the last half cut-off length.[34] It is also important to note that the Gaussian filter used here is designed to have a transmission ratio of 50% at $\lambda_c$. This allows to calculate the waviness profile by simply subtracting the roughness from the primary profile.[34]

### 2.4. Determination of surface parameters

In order to provide a numerical evaluation of the surface, quantitative parameters can be calculated either on the straightened primary profile, or on the roughness/waviness profiles (based on the mean line produced by the filtering). The complexity of the surface or interface can be simply evaluated by the ratio of the developed length ($L_d$) along the profile to the projected length ($L_p$) on the $x$-axis (i.e. the length of the image-field). This dimensionless criterion $L_d/L_p$, expressed "in excess" relative to 100%, reflects in fact the "tortuosity" of the primary profile. However, it can be regarded as a "fractal dimension", since its value may also depend on the image resolution. A sensitivity analysis was performed on SEM images sizing (712 × 484) pixels,[2] acquired on the ceramic sample at various magnification factors ranging from ×500 to ×1250 (and therefore various spatial resolutions). A similar profile length is extracted at the same position on each image, in order to determine the tortuosity ratio $L_d/L_p$ (Table 1). One can observe that $L_d/L_p$ slightly increases with the image resolution, but not really significantly for the investigated magnifications (coefficient of variation lower than 1%). Nevertheless, it should be recommended to consider this parameter only when comparing images with an equivalent spatial resolution.

2D roughness and waviness parameters used hereafter, whose complete definition can be found in ISO 4287,[36] are calculated on the filtered profiles. The asperity height of the roughness profile is quantified by amplitude parameters (such as $R_a$, $R_z$, $R_t$, $R_q$, etc...), all expressed in micrometers. As an example, the mean roughness ($R_a$) measures the arithmetical average of the absolute values of the profile height deviation from the mean line on the evaluation length. It can be expressed in the discrete case as:

$$R_a = \frac{1}{n}\sum_{i=1}^{n} |z_i| \quad (9)$$

where $n$ is the number of data points on the evaluation length $l_e$, and $z_i$ the distance between the height of point $i$ and the mean line.

The root-mean-square roughness (*RMS* or $R_q$) calculates the root mean square average of the profile height deviations from the mean line (i.e. the standard deviation of the height distribution):

$$R_q = \sqrt{\frac{1}{n}\sum_{i=1}^{n} z_i^2} \quad (10)$$

The total height of the roughness (respectively waviness) profile, $R_t$ (resp. $W_t$), measures the height between the highest peak ($R_p$) and the deepest valley ($R_v$) within the evaluation length:

$$R_t = \left|\max(R_{pi})\right| + \left|\max(R_{vi})\right| \quad (11)$$

The peak density ($RP_c$) is a spacing parameter which consists in counting the number of peaks over the evaluation length, and normalizing it on a length of 1 cm. A peak is counted each time

Table 2
Standardized roughness parameters measured by mechanical profilometry on $Si_3N_4$-TiN samples oxidized at 1150 °C in air for various durations (mean values calculated on 51 profiles).

| Oxidation time | Roughness parameters (μm) | | | | | | | | |
|---|---|---|---|---|---|---|---|---|---|
| | $R_a$ | $R_q$ | $R_z$ | $R_{max}$ | $R_t$ | $R_p$ | $R_v$ | $RS_m$ | $RP_c$ |
| 1 h | 1.37 | 1.77 | 10.7 | 13.0 | 13.7 | 7.35 | 3.35 | 26.1 | 32.7 |
| 10 h | 2.00 | 2.61 | 13.5 | 15.7 | 16.0 | 10.2 | 5.80 | 34.0 | 28.8 |
| 50 h | 2.30 | 2.91 | 15.4 | 18.0 | 18.7 | 7.20 | 7.30 | 35.0 | 30.1 |
| 100 h | 2.83 | 3.56 | 18.3 | 21.2 | 22.0 | 13.3 | 8.30 | 83.0 | 24.5 |

the profile consecutively crosses the lower ($C_2$) and upper ($C_1$) cutting depths, placed symmetrically on either side of the mean line (here considered at ±1 μm).

The mean spacing of irregularities ($RS_m$) defines the mean value of the width $XS$ of the profile elements (consisting in a profile peak and the adjacent valley):

$$RS_m = \frac{1}{m}\sum_{i=1}^{m} XS_i \quad (12)$$

where $m$ is the number of profile elements within the evaluation length.

$RS_m$ gives the length of the period in the case of a periodic or pseudo-periodic profile.

The skewness of the profile ($RS_k$) is the quotient of the mean cube value of the ordinate values $z(x)$ and the cube of $R_q$ within the evaluation length:

$$RS_k = \frac{1}{{R_q}^3}\left(\frac{1}{n}\sum_{i=1}^{n} z_i^3\right) \quad (13)$$

$RS_k$ is an adimensional parameter which provides a description of the asymmetry of the profile. $RS_k$ is close to zero for a Gaussian heigth distribution, whereas a positive value indicates a flat surface with peaks, and a negative value a bearing surface with valleys.

## 3. Validation of the method

To assess the reliability and performance of the roughness quantification using image analysis, comparative measurements were performed by conventional profilometric technics. For this purpose, three $Si_3N_4$–TiN ceramic samples thermally aged at 1150 °C in air for various exposure times (from 1 to 100 h) and providing different surface qualities of the superficial oxide layer, are characterized. 2D roughness parameters are determined according to ISO 4287.[36]

### 3.1. Measurements by stylus profilometry

Mechanical (or stylus) profilometry consists in traversing at a constant velocity across the surface to measure with a stylus, whose vertical displacement is converted into an electric signal using an inductive transducer, and electronically amplified. The diamond tip stylus is cone shaped, with a 5 μm radius and a 90° angle. The measuring range of the skidless pick-up is ±100 μm, and its vertical resolution (along $z$-axis) is 10 nm. A scanning length $l_t$ of 4.8 mm is selected, with a sampling interval of 1 μm. Fifty-one profiles, distant from 50 μm each other, are scanned over the sample surface. Each profile is straightened by least-squares regression, in order to correct the misalignment of the measured surface with the reference plane of the traverse unit. Then, the leveled profiles are filtered by using an appropriate cut-off length ($\lambda_c$ = 0.8 mm here), and roughness parameters are calculated (Table 2).

It must be emphasized that the stylus curvature radius, which acts as a mechanical low-pass filter, produces a smoothing of the real surface.[37] This results in the loss of high spatial frequencies (narrow crevices and sharp peaks) on the profile (Fig. 4). Thus, using a 5 μm/90° tip, the surface features having an angle greater than 45° to the horizontal and crevices which are narrower than 10 μm cannot be accurately recreated. Therefore, roughness parameters such as the total height $R_t$ or the maximal height $R_{max}$ determined from mechanical probe measurements are always underestimated.

### 3.2. Measurements by optical profilometry

The same ceramic samples are measured using an extended field confocal microscope AltiSurf520 (from Altimet®), which is an optical profiler based on the principle of chromatic coding. A white-light source is focused on the sample surface where it is reflected, and a chromatic lens splits the reflected signal into its constituent wavelength. The exact height of the focused point is converted by a spectrometer. A chromatic (350 μm range) sensor, with an axial resolution of 10 nm and a lateral resolution of 4 μm, is used. A rectangular area of 4.8 mm × 2.5 mm is scanned with a sampling interval of 1 μm, a scanning speed of 1 mm/s and a sampling frequency of 1000 Hz, providing a 3D topographical view of the sample surface (Fig. 5). Roughness parameters, calculated on 501 profiles extracted on the 3D surface, are reported in Table 3.

### 3.3. Measurements by image analysis

For each sample, the profile of the oxide layer is detected by image analysis on a series of 36 contiguous SEM images, by applying the processing routine detailed in Fig. 2. The profiles extracted from each image are saved in an *ASCII* file, as a list of points with a spatial resolution of 0.25 μm. Then, the profiles are mathematically processed following the procedure detailed in Fig. 3. However, in order to compare these results with those obtained by mechanical profilometry, an algorithm was developed to reproduce the "smoothing" effect of the stylus. The moving of a ball with a radius curvature of 5 mm is simulated

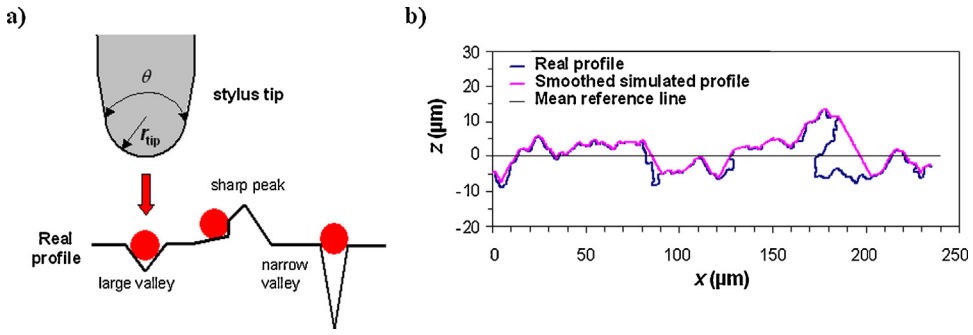


Fig. 4. Limitations of contact measurements, due to the mechanical low-pass filtering exerted by the stylus tip geometry: (a) simulation of the effect of the tip radius on the surface profile; (b) smoothed profile by removing shorter frequencies corresponding to sharp peaks and narrow valleys.

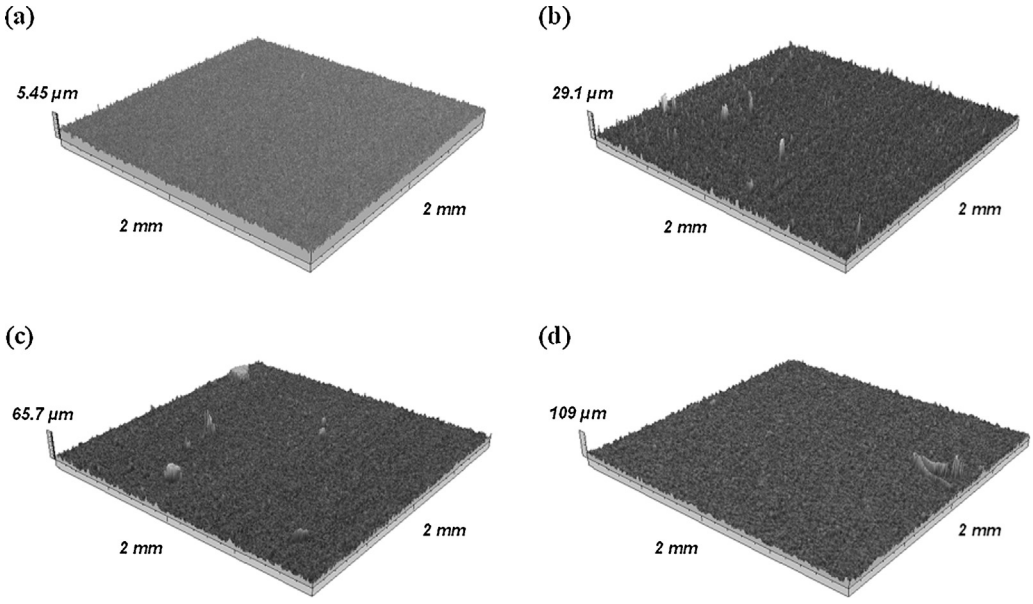


Fig. 5. Topographies of $Si_3N_4$–TiN ceramic samples performed with an extended field confocal microscope (only a partial view of 2 mm × 2 mm is shown in order to better highlight surface defects): unaged polished ceramic (a); top oxide layer formed after aging at 1150 °C in air for 1 h (b), 10 h (c) and 100 h (d).

over the rough surface, in order to filter the surface asperities that cannot be detected by the conical probe tip (Fig. 4a). Then, the resulting "smoothed" profile is leveled and filtered using a Gaussian numerical filter.

Roughness parameters are calculated on profiles processed or not with the smoothing algorithm, as reported in Table 4. It can be observed that the smoothing of the profile slightly changes the parameter values, especially for rougher surfaces and spacing parameters ($RS_m$, $RP_c$). Globally, the amplitude parameters are lowered (except average parameters such as $R_a$ and $R_q$), while the mean spacing of profile irregularities ($RS_m$) is increased due to the loss of fine details in the surface profile.

### 3.4. Reliability and precision of the method

In Table 5 are reported the mean relative differences on roughness parameters between measurements performed by image analysis and by conventional techniques (stylus and optical profilometry). As can be noted, the results provided by the image analysis method are closer to those obtained by white light

Table 3
Standardized roughness parameters measured by white light confocal microscopy on $Si_3N_4$–TiN samples oxidized at 1150 °C in air for various durations (mean values calculated on 501 profiles).

| Oxidation time | Roughness parameters (µm) | | | | | | | | |
|---|---|---|---|---|---|---|---|---|---|
| | $R_a$ | $R_q$ | $R_z$ | $R_{max}$ | $R_t$ | $R_p$ | $R_v$ | $RS_m$ | $RP_c$ |
| 1 h | 1.50 | 1.99 | 12.2 | 17.2 | 19.2 | 8.80 | 3.07 | 30.4 | 22.2 |
| 10 h | 2.45 | 3.15 | 18.4 | 28.2 | 32.9 | 12.3 | 5.79 | 31.0 | 26.2 |
| 50 h | 2.98 | 3.63 | 20.3 | 24.7 | 27.4 | 11.7 | 8.28 | 30.0 | 27.9 |
| 100 h | 4.03 | 5.24 | 29.1 | 37.0 | 35.8 | 15.5 | 11.6 | 37.2 | 24.8 |

Table 4
Standardized roughness parameters measured by image analysis on SEM cross-sections of oxidized $Si_3N_4$–TiN samples at 1150 °C.

| Oxidation time | "Smoothing" algorithm | Roughness parameters (μm) | | | | | | | | |
|---|---|---|---|---|---|---|---|---|---|---|
| | | $R_a$ | $R_q$ | $R_z$ | $R_{max}$ | $R_t$ | $R_p$ | $R_v$ | $RS_m$ | $RP_c$ |
| 1 h | No | 1.57 | 2.14 | 12.5 | 16.2 | 16.8 | 9.98 | 3.14 | 24.3 | 26.6 |
| | Yes | 1.64 | 2.21 | 12.4 | 15.9 | 16.5 | 9.64 | 3.24 | 32.6 | 22.4 |
| | *Relative difference (%)* | *4.5* | *3.1* | *−0.7* | *−2.0* | *−2.0* | *−3.4* | *3.2* | *33.9* | *−15.8* |
| 10 h | No | 2.61 | 3.42 | 19.5 | 25.8 | 26.8 | 14.8 | 5.61 | 30.4 | 29.4 |
| | Yes | 2.68 | 3.47 | 18.8 | 25.7 | 24.6 | 13.9 | 5.82 | 38.0 | 22.4 |
| | *Relative difference (%)* | *2.6* | *1.5* | *−3.9* | *−4.6* | *−4.1* | *−5.8* | *3.7* | *24.7* | *−23.8* |
| 50 h | No | 2.88 | 3.62 | 19.9 | 23.7 | 26.9 | 12.2 | 7.04 | 33.5 | 24.5 |
| | Yes | 2.85 | 3.56 | 18.5 | 22.4 | 23.7 | 11.3 | 6.56 | 41.6 | 19.7 |
| | *Relative difference (%)* | *−1.0* | *−1.7* | *−7.2* | *−5.1* | *−11.9* | *−7.8* | *−6.9* | *23.9* | *−19.6* |
| 100 h | No | 3.71 | 4.54 | 24.2 | 29.1 | 36.9 | 12.6 | 12.4 | 44.6 | 19.9 |
| | Yes | 3.98 | 4.74 | 25.0 | 26.1 | 26.5 | 12.0 | 11.0 | 53.0 | 16.7 |
| | *Relative difference (%)* | *7.3* | *4.4* | *3.1* | *−10.2* | *−28.1* | *−4.8* | *−11.4* | *18.9* | *−16.0* |

extended field confocal microscopy (with a difference always less than 20% and 10% on average). The difference found with the stylus profiler is greater, image analysis giving higher values of about 30% on average (and up to 60% on $R_t$), despite the smoothing of the profile simulating the conical tip of the stylus. This result can be explained by the higher spatial resolution reached on the SEM images (0.25 μm instead of 1.2 μm for the stylus), as it is also the case for the optical sensor (4 μm). This offsets the lower resolution along $z$ axis (25 times larger than the theoretical axial resolution of conventional methods). In addition, the fineness of detail reproduction is much better, as profile irregularities corresponding to "backtracking" can be restored (Figs. 2f and 4b). On the other hand, it should be emphasized that some errors may be introduced during the metallographic preparation of the sample. Thus, cutting and polishing operations can locally cause tearing of the outer surface, resulting in a slight modification of the surface. This is especially true when the material is brittle, as often the case with an oxide layer. However, such artefacts of preparation have a null or minor influence on the reproduction quality of the internal (sub-layer) interfaces, which are the final subject of this study. Anyway, the particularly good agreement with optical measurements indicates that roughness parameters can be evaluated with satisfying orders of magnitude with our method. In addition, evolution of the roughness of the ceramic composite surface as a function of oxidation time is clearly highlighted, as shown in Fig. 6.

## 4. Application to a thermally aged ceramic composite: effect of the "roughening" of the internal oxidation interface on the mechanical strength

### *4.1. Material and experimental procedure*

The material is a silicon nitride ($Si_3N_4$) based ceramic containing 30% volumic of titanium nitride (TiN) particles, named Kersit 601, and elaborated by powder sintering. This low-density composite material is a good candidate to replace molybdenum superalloys – which are very expensive and very reactive with oxygen – in hot forging dies operating at temperatures above 1000 °C. Indeed, its good thermal properties (low thermal expansion coefficient, high thermal conductivity), associated with high mechanical and corrosion resistances, make it suited to withstand sudden temperature changes in service.[38]

In order to study the oxidation behavior of the ceramic composite, static isothermal tests are performed at 1150 °C in air on small samples with a polished surface ($R_a = 0.23$ μm), for various times (from 1 h to 200 h). Then, the thermally aged samples are prepared as cross sections, and observed with SEM

Table 5
Comparison of the roughness parameters measured by image analysis and by conventional methods.

| Oxidation time | Reference (conventional profilometric method) | Relative difference (%) on calculated roughness parameters | | | | | | | | |
|---|---|---|---|---|---|---|---|---|---|---|
| | | $R_a$ | $R_q$ | $R_z$ | $R_{max}$ | $R_t$ | $R_p$ | $R_v$ | $RS_m$ | $RP_c$ |
| 1 h | Mechanical (stylus) | 19.9 | 24.7 | 15.4 | 22.1 | 20.4 | 31.0 | −3.4 | 24.8 | −31.6 |
| | Optical (confocal micr.) | 4.9 | 7.4 | 2.0 | −5.7 | −12.6 | 13.5 | 2.1 | −20.0 | 19.8 |
| 50 h | Mechanical (stylus) | 33.8 | 33.0 | 39.0 | 56.4 | 60.6 | 36.7 | 0.3 | 11.6 | −22.2 |
| | Optical (confocal micr.) | 6.5 | 8.7 | 6.1 | −8.6 | −18.4 | 20.7 | −3.0 | −2.0 | 12.2 |
| 50 h | Mechanical (stylus) | 23.9 | 22.3 | 20.2 | 24.7 | 26.7 | 56.7 | −10.1 | 18.8 | −34.6 |
| | Optical (confocal micr.) | −3.2 | −0.2 | −1.7 | −4.2 | −1.8 | 4.2 | −14.9 | 12.0 | −12.2 |
| 100 h | Mechanical (stylus) | 40.6 | 33.1 | 36.4 | 23.2 | 20.5 | −9.8 | 31.9 | −36.1 | −31.8 |
| | Optical (confocal micr.) | −8.0 | −13.4 | −16.7 | −18.8 | −7.4 | −18.8 | 6.6 | 19.7 | 19.9 |

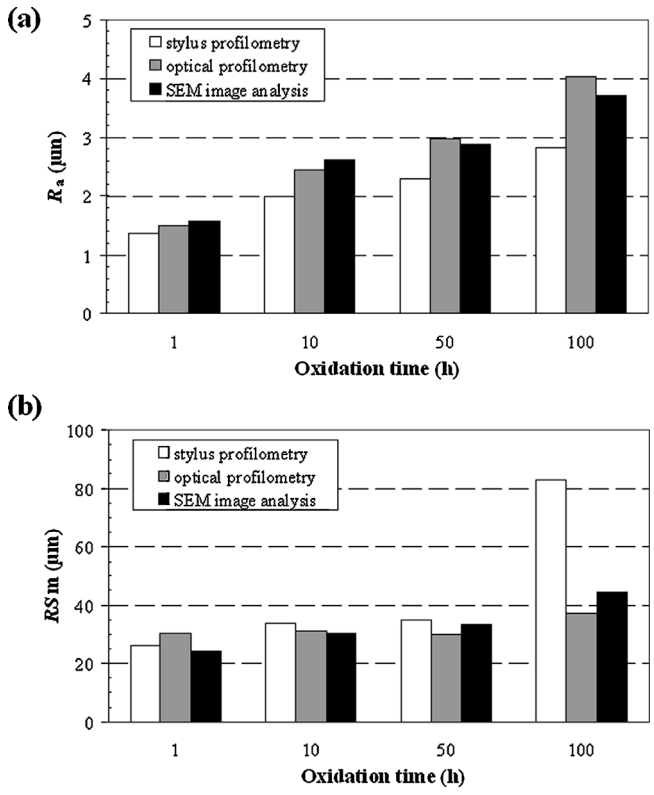


Fig. 6. Comparative evolution of roughness parameters measured by image analysis and conventional methods (mechanical and optical profilometry) on the surface oxide layer of oxidized ceramic samples at 1150 °C, vs. oxidation time: (a) mean roughness $R_a$; (b) mean spacing of profile irregularities $RS_m$.

using a BSE detector. The oxidation mechanisms and kinetics are fully described in.[38] As shown in Fig. 7, two oxidation layers of different nature and composition are formed:

- a very compact and quasi-continuous top layer, consisting mainly of $TiO_2$ (appearing in light gray) with lesser amounts of a $SiO_2$ glassy phase (in mid gray),
- a porous sub-surface layer partially oxidized, consisting of titanium oxide and silicon oxynitride (appearing in dark gray), which overcomes the two-phase core material (with TiN grains in white and $Si_3N_4$ matrix in mid gray).

In parallel to the oxidation tests, four-point bending tests are performed at 1150 °C on parallelepiped polished specimens, pre-oxidized at 1150 °C in air for various durations, in order to determine the failure strength of the material according to the oxidation duration. An electromechanical press Instron 5800 with a maximum load capacity of 30 kN, equipped with a tubular resistance furnace, is used. After holding the specimens at 1150 °C for various times (from 30 min to 100 h), the bending tests are performed with a speed of 0.2 mm/s until failure. At the end of the test, the specimen is cooled to room temperature at a rate of 10 °C/min, in order to avoid thermal shock.

The maximum stress experienced by the specimen is given by:

$$\sigma_{\max} = \frac{3}{2}\frac{P(L-l)}{bh^2} \tag{14}$$

where $P$ is the applied load (in N), $L$ and $l$ are the distances between upper and lower supports (40 mm and 20 mm, respectively) in the bending test, and $b$ and $h$ are the width and the thickness of the specimen (4 mm and 3 mm, respectively).

Fig. 5 clearly indicates that the surface roughness of thermally aged $Si_3N_4$–TiN samples increases due to oxide growth. This "roughening" can be quantified by image analysis. The profile of the top oxide layer is extracted on each field of the series of contiguous cross-sectional SEM images, by applying the processing algorithm described above (Fig. 2). Another algorithm is developed to detect the interface between the partially oxidized area and the bulk ceramic, based on their difference in microstructure. It consists of four steps, as detailed in Fig. 8:

(a) dilatation to expand the white grains (TiN phase) in the non-oxidized area (Fig. 8a);
(b) thresholding of the gray levels corresponding to the undamaged area, composed of white TiN grains relatively large (Fig. 8b);

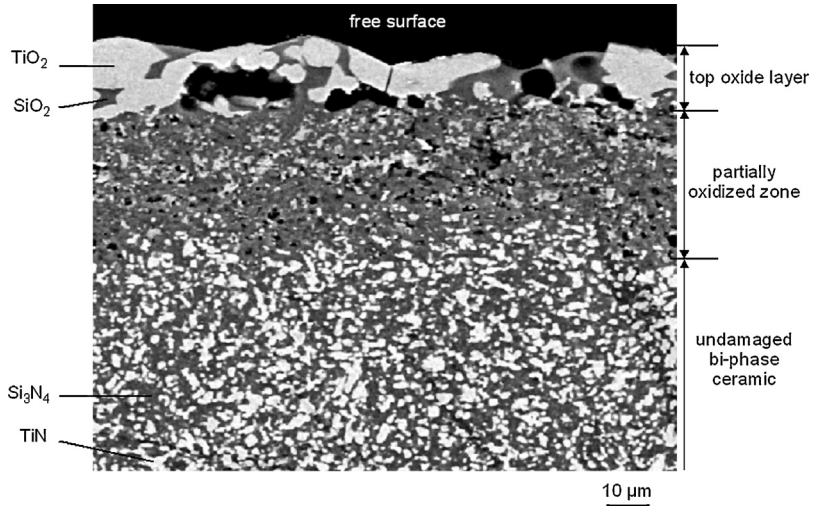


Fig. 7. Oxidation layer formed on a $Si_3N_4$–TiN composite ceramic thermally aged at 1150 °C in air, observed in cross-section with SEM using a BSE detector.

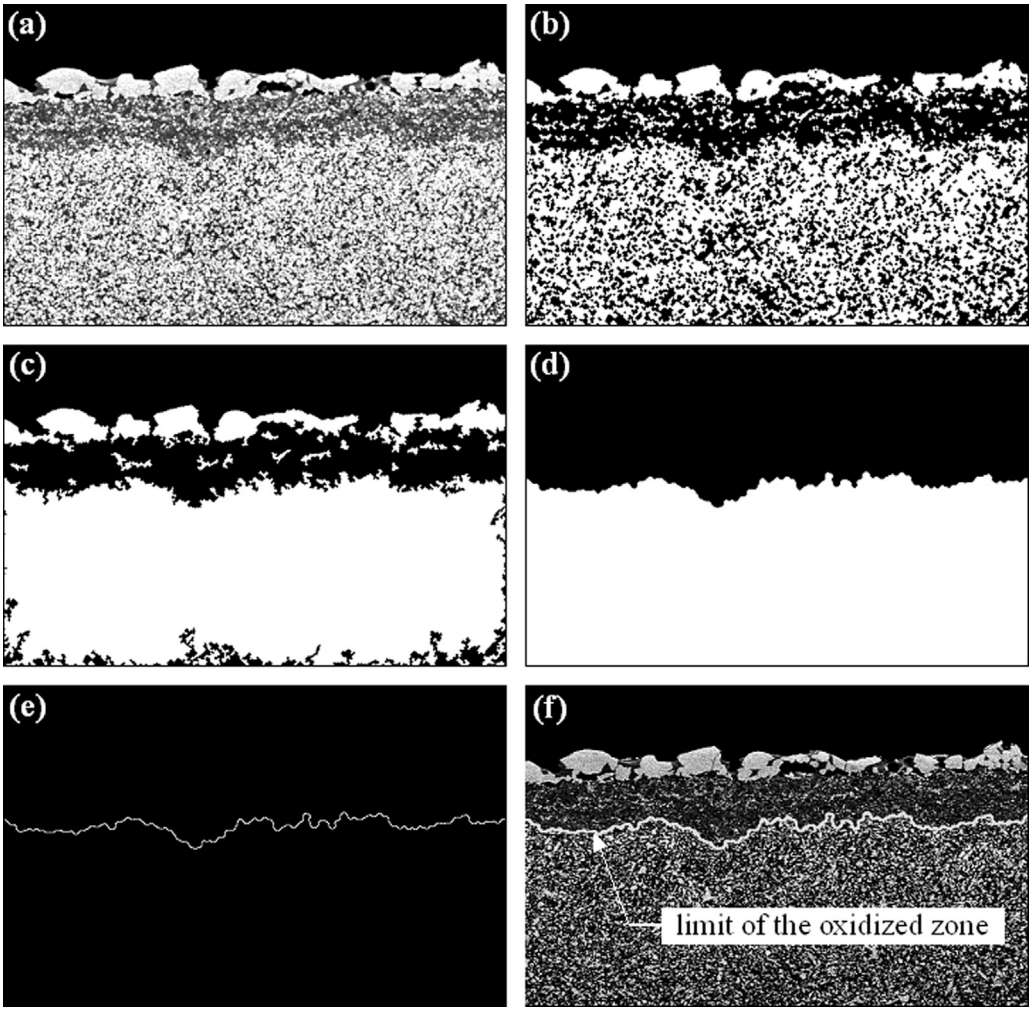


Fig. 8. Image analysis procedure applied on the image of Fig. 2b, to detect the interface between the partially oxidized zone and the undamaged ceramic: (a) dilatation of size 1 to expand the white grains (TiN phase) in the non-oxidized area; (b) thresholding of the light intensities in the image (a); (c) morphological closing to connect the closest binary TiN grains; (d) detection of the non-oxidized area by mathematical morphology operations (hole-filling, erosion-reconstruction to remove the binary noise, and smoothing of the contour of the detected area by series of closing-opening); (e) extraction of the interface profile by logical difference between the image (d) and its eroded of size 1; (f) interface profile superimposed on the initial SEM image.

(c) connection of the closest thresholded grains and removing of the binary noise, using mathematical morphology operations (Fig. 8c and d);
(d) detection of the profile of the upper interface of the undamaged area by a logical difference between the previous binary image and its eroded of size 1 (Fig. 8e).

Primary (unfiltered) profiles resulting from the image processing of the samples for various oxidation times are reported on Fig. 9a and b, respectively for the upper oxide layer and the interface between the partially oxidized zone and the bulk ceramic.

### 4.2. *Results and discussion*

The thickness of the top oxide layer and of the partially oxidized area increases by increasing the oxidation time (Fig. 10). Fig. 9a shows that the initially smooth surface develops roughness defects whose amplitude increases during oxidation, as better reflected by the increasing trend versus oxidation time of the average surface roughness $R_a$ (Fig. 11a). A gradual roughening is also observed at the interface between the partially oxidized area and the undamaged substrate, and especially beyond 10 h of oxidation (Figs. 9b and 11a).

Due to the brittle nature of the ceramic material, the results of the bending tests are represented by the failure probability (Weibull distribution) as a function of the maximum stress suffered by pre-oxidized specimens for 0.5 h, 50 and 100 h (Fig. 12). As could be expected, the rupture probability is much higher when the oxidation time is longer and the tensile strength is reduced by about 100 MPa when the oxidation time is increased to 100 h. The decrease of the mean failure stress is then correlated to the increase of $R_a$ at the interface between the partially oxidized area and the bulk ceramic during oxidation (Fig. 11a), that causes an increase of stress concentrations at the surface of the bulk material. The increased amplitude of waviness defects, maximum after 100 h (Fig. 11b), can also contribute to amplify this stress concentration effect, even if those higher wavelength

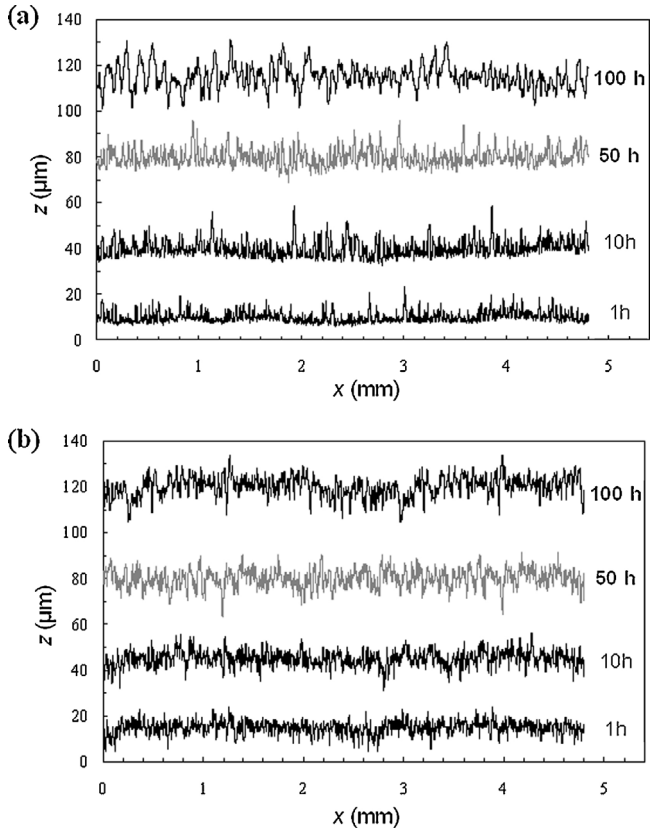


Fig. 9. Evolution the profile of the superficial oxide layer (a) and of the interface between the partially oxidized area and the bulk ceramic (b), for various oxidation times at 1150 °C (the profiles are vertically offset).

defects may produce a lesser "notch effect".[39] It is well known that for brittle materials, the failure strength is directly correlated to surface or volume flaws distribution in the material. In the case of high strength $Si_3N_4$–TiN ceramic composites, surface flaws become more critical than volume flaws when surface roughness increases. As observed in Fig. 7, the partially oxidized sub-layer is very porous, lowering its strength as compared to that of the bulk material. This is confirmed by the occurrence of oxide spallation generally observed along the interface between the bulk ceramic and the partially oxidized layer on post-mortem

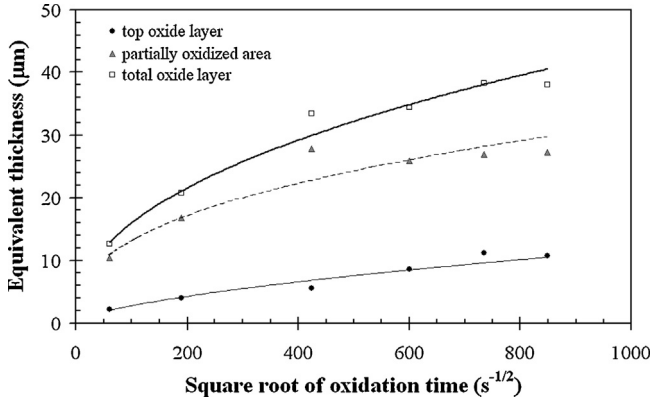


Fig. 10. Oxidation kinetics of the $Si_3N_4$–TiN ceramic under thermal aging tests in air at 1150 °C.

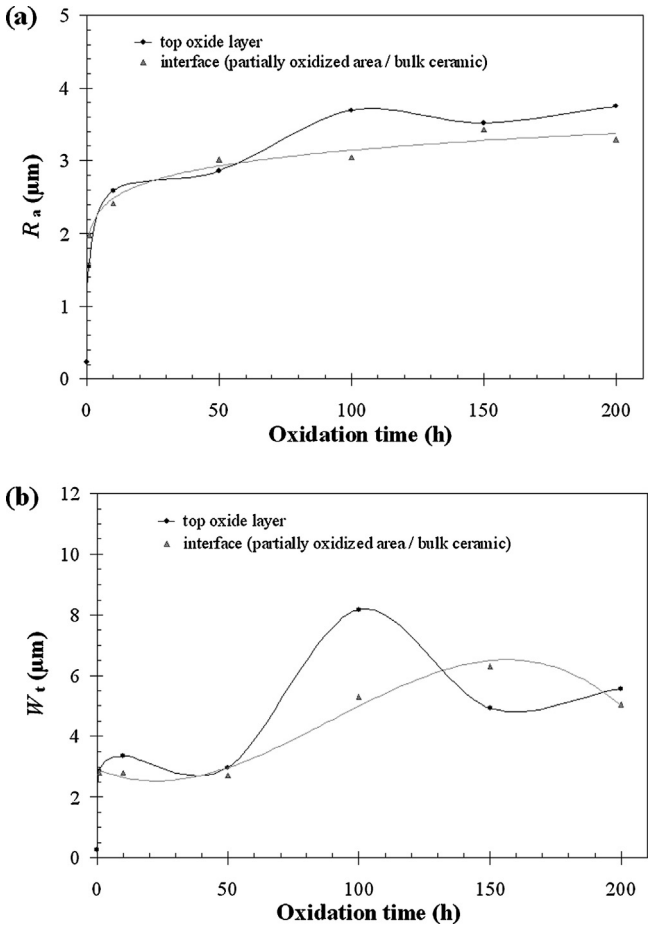


Fig. 11. Variation with the oxidation time of the profile irregularity of the top oxide layer and at the interface between the partially oxidized area and the bulk ceramic: (a) mean roughness $R_a$; (b) waviness depth $W_t$.

bending specimens. Then, we can suppose that the surface flaws responsible for the decrease of the failure strength of oxidized materials are located at the bulk material/partially oxidized zone interface. In addition, Fig. 12 indicates that dispersion of failure

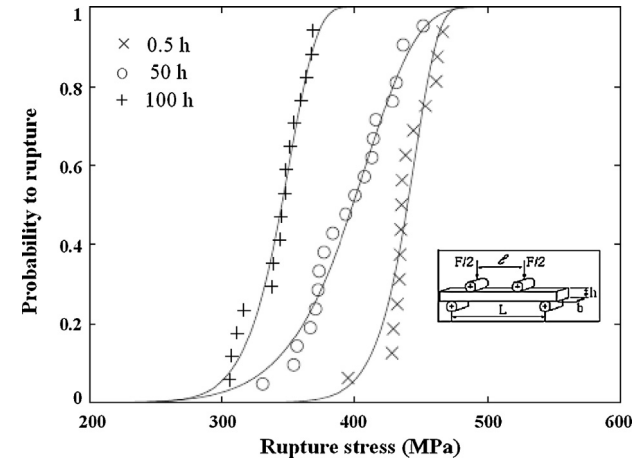


Fig. 12. Results of the room temperature 4-points bending tests performed on $Si_3N_4$–TiN specimens pre-oxidized at 1150 °C during 0.5 h, 50 and 100 h: graphic representation of the probability of failure as a function of the rupture stress.

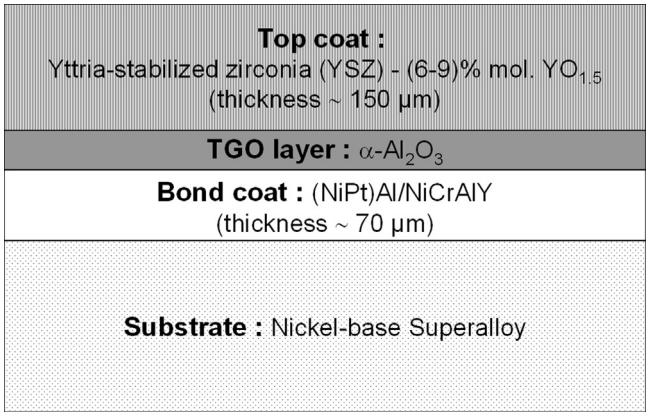


Fig. 13. Laminate structure and composition of the thermal barrier coatings elaborated by EB-PVD process.

stresses increases after 50 oxidation hours, and then decreases after 100 h. This can be related to the density of large surface flaws that systematically provokes fracture under low stress for long term exposure. As can be observed on the surface profiles of Fig. 9a, such surface defects are more numerous after 100 oxidation hours, increasing the risk of failure and thus reducing the fracture stress dispersion. On the contrary, there are few deep valleys after 50 hours exposure, which lowers the probability for initiating cracks on surface defects and explains the experimental values significantly scattered on the Weibull distribution.

## 5. Application to the oxidation of thermal barrier coating systems: relationship between the ratcheting of the thermally grown oxide and the interfacial adhesion

### *5.1. Material and experimental procedure*

The investigated material is a thermal barrier coating (TBC) system deposited by EB-PVD (Electron-Beam Physical Vapour Deposition) on a nickel based superalloy substrate. The EB-PVD coating consists of three superposed layers (Fig. 13):

- a ceramic top coat of ~7% yttria-stabilized zirconia, acting as a thermal barrier,
- a slowly growing, adherent α-$Al_2O_3$ thermally grown oxide (TGO), acting as a diffusion barrier,
- an alumina-forming (Ni,Pt)Al bond coat, which accomodates the differences in thermal expansion between the superalloy and the thermal barrier, thus enhancing the adherence of the top-coat.

Such TBC systems are used in the manufacture of aircraft engine blades, and especially in jet engine turbines to protect single crystal blades from both the corrosive attack of combustion hot gases and the extremely high temperature continuously increased to enhance engine efficiency. In service, this complex multi-layered structure is exposed to severe conditions, and the resulting thermo-mechanical loading is responsible for the degradation of the interfacial adhesion of the layers which may lead to a premature damage of the component.

We aim to investigate the thermal aging of the TBC system under static isothermal conditions, for 100 h at oxidation temperatures ranging from 1050 to 1150 °C. We focus on the alumina TGO layer, initially formed by the oxidation of aluminum drawn from the reservoir bond coat in contact with the oxygen of air. Indeed, the time and temperature dependent thickening of this layer during thermal aging or cycling develops significant growth stress as well as rumpling and associated strain, possibly leading or at least contributing to the spallation of the thermal barrier coating. To assess the effect of the temperature on both the thickness and the wrinkling of the TGO layer, the thermally aged samples are prepared as cross-sections and observed in SEM (Fig. 14). The interfacial roughness of the TGO layer is quantified using Aphelion® on a series of 30 images-fields sizing $(2048 \times 1887)$ pixels$^2$ and aquired over a total length of 4.8 mm with a magnification of 750×. The image analysis algorithm, detailed in Fig. 15, is composed of several steps including:

(a) a median filtering of the initial SEM image (Fig. 15a);
(b) the thresholding of the dark gray levels corresponding to the TGO layer. As can be observed in Fig. 15b, some dark precipitates in the superalloy and big porosities in the upper ceramic are also detected;
(c) an hysteresis thresholding selecting only the precipitates and porosities (Fig. 15c);the removing of the binary noise by a logical difference between the images of Fig. 15b and Fig. 15c. One can note that even if some unwanted details still remains in Fig. 15d, it is disconnected from the layer of interest. The complete removal of residual noise is achieved by erosion-reconstruction with a structuring element of appropriate size, which allows the detection of the single layer (Fig. 15e);
(d) the extraction of both upper and lower profiles of the TGO layer by logical difference between the binary image of the layer and its eroded of size 1 (Fig. 15f). The upper ($P_u$) and lower ($P_l$) profiles correspond to the interface between the TGO layer and the ceramic layer, and between the TGO layer and the sub-layer covering the superalloy substrate, respectively.

The equivalent thickness ($t_e$) of the TGO layer can be calculated by dividing the area $A$ of the layer (number of binarized pixels in the image of Fig. 15e) and the developed length $L_m$ (in pixels) of the median profile of the layer, as expressed by:

$$t_e = (A/L_m)r \quad (15)$$

Note that the result is calibrated, knowing the spatial resolution of the image ($r = 0.083$ µm/pixel here).

As detailed in Fig. 16, the median axis (line of 1 pixel width) is achieved by skeletonization of the TGO layer, followed by a pruning to convergence to remove the residual barbules of the skeleton.[30] Taking into account the median length $L_m$ (instead of the projected length $L_d$) in Eq. (15) provides a more accurate estimation of the mean thickness of the TGO layer, since the median axis better reflects the "ratcheting effect"of the layer. In

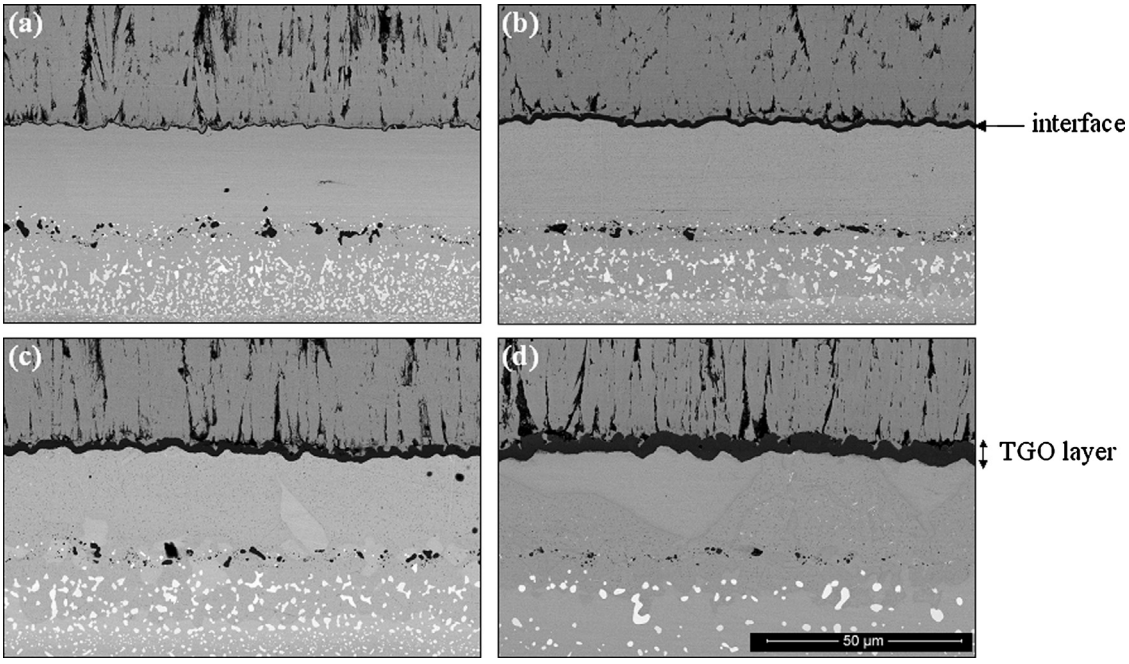


Fig. 14. SEM observations showing the increased thickness and roughening of the TGO layer due to thermal aging: reference unaged sample (a) and thermally aged samples at 1050 °C (b), 1100 °C (c), and 1150 °C (d).

addition, the linear density of barbules ($d_b$) along the profile is calculated as:

$$d_b = N_b / L_d \tag{16}$$

where $N_b$ is the number of barbules of significant size (>1 μm here).

In parallel, interfacial Vickers indentation are implemented, in order to determine the critical load required to initiate crack between the ceramic and the TGO layer and consequently to characterize the adhesion of the TBC system on the substrate material. The critical load is approached by first establishing both the "hardness master curve" and the "crack curve", plotting respectively the indent size and crack size versus the applied force. It is then determined graphically by seeking the intercept, for each aging condition, between the two curves.[40] In turn, the apparent toughness of the interface is calculated using the following expression:

$$K_{ca} = 0.015 \frac{P_c}{{a_c}^{3/2}} \left(\frac{E}{H}\right)_i^{1/2} \quad \text{and} \quad \left(\frac{E}{H}\right)_i^{1/2} = \frac{\left(\frac{E}{H}\right)_S^{1/2}}{1 + \left(\frac{H_S}{H_{TBC}}\right)_i^{1/2}} + \frac{\left(\frac{E}{H}\right)_{TBC}^{1/2}}{1 + \left(\frac{H_{TBC}}{H_S}\right)_i^{1/2}}, \tag{17}$$

where subscript $S$, $i$ and TBC stands respectively for the substrate, the interface and the TBC, $P_c$ is the critical load (in N), $a_c$ is the crack length (in m) at the critical load, $E$ is the Young modulus (200 GPa for the substrate, and 66 GPa for the TBC coating), $H$ is the hardness (550 HV, i.e. 5.39 GPa for the substrate, and 401 HV, i.e. 3.93 GPa for the TBC coating).

### 5.2. Results and discussion

As shown in Fig. 13b–d, the TGO layer grows and significantly changes its morphology upon isothermal oxidation. However, its upper ($P_u$) and lower ($P_l$) interfaces do not exhibit the same evolution, $P_u$ becoming progressively more corrugated than $P_l$ as oxidation temperature is increased. To quantify this morphological evolution, a normalized rumpling index (*NRI*) is defined as the ratio of the fractal parameter $L_d/L_p$ (as detailed in Section 2.4) measured after thermal aging and initially before any temperature exposure:

$$\text{NRI} = \frac{(L_d/L_p)_{\text{aged}}}{(L_d/L_p)_{\text{unaged}}} \tag{18}$$

Fig. 17 reveals that an increase in the oxidation temperature from 1050 to 1150 °C results in a roughly linear increase of the *NRI* value, in particular at the interface between the TGO layer and the ceramic top coat. The roughening of the interface is also highlighted by the root-mean-square roughness $R_q$ (Fig. 18a), whose evolution indicates that the amplitude of defects is strongly increased under the effect of the aging temperature, and especially above 1150 °C. A detailed statistical analysis further reveals that the distribution of defects changes along the TBC–TGO interface, as shown by the evolution of the skewness $RS_k$ (which expresses the asymmetry of the profile relative to the mean line) versus the temperature (Fig. 18b). $RS_k$ changes from initially near zero for the unaged sample to a negative value for thermally aged samples. It can thus be inferred that the morphology of the TGO layer evolves by formation of deeper "valleys" (inward defects) upon thermal aging.

All these observations globally reflects an enhancement of the tortuosity of the interface between the TBC and the TGO

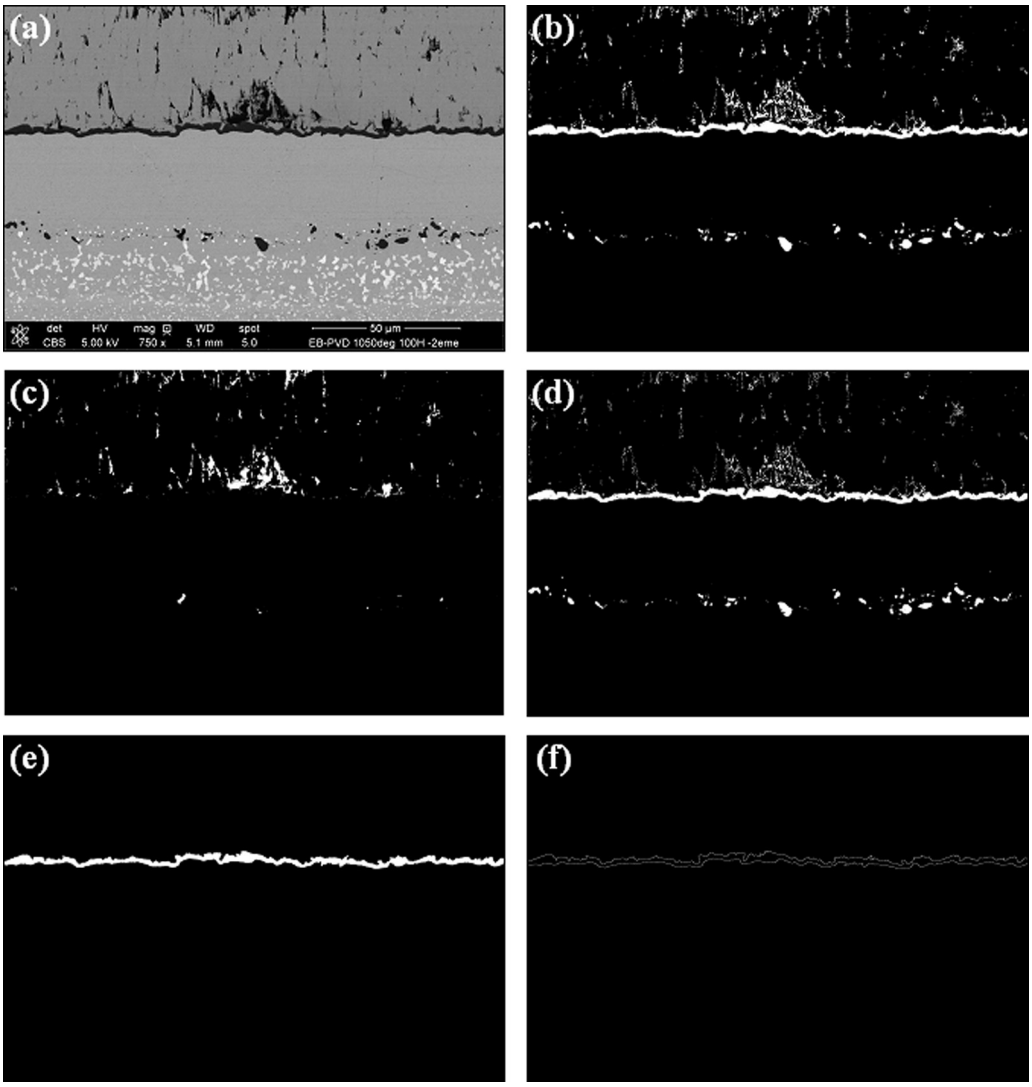


Fig. 15. Image analysis procedure to extract the upper and lower profiles of the TGO layer: (a) median filtering of the SEM image; (b) thresholding of the TGO layer; (c) thresholding of the precipitates "connected" to the TGO layer; (d) logical difference between images (b) and (c); (e) erosion-reconstruction of the image (d) to filter the binary noise; (f) detection of the profiles by logical difference between the image (e) and its eroded of size 1.

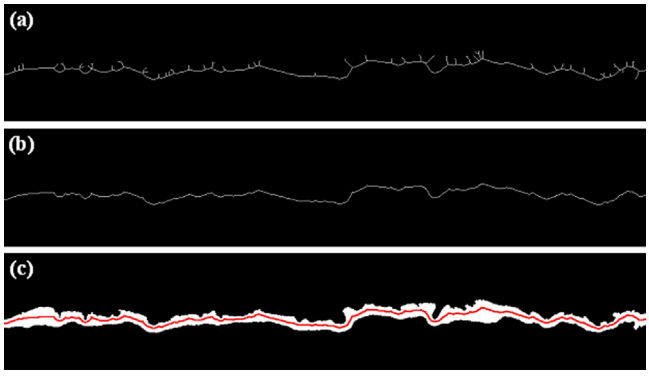


Fig. 16. Detection of the median axis of the TGO layer: (a) skeletonization of the layer; (b) pruning of the skeleton to remove residual barbules; (c) superimposition of the median profile on the TGO layer.

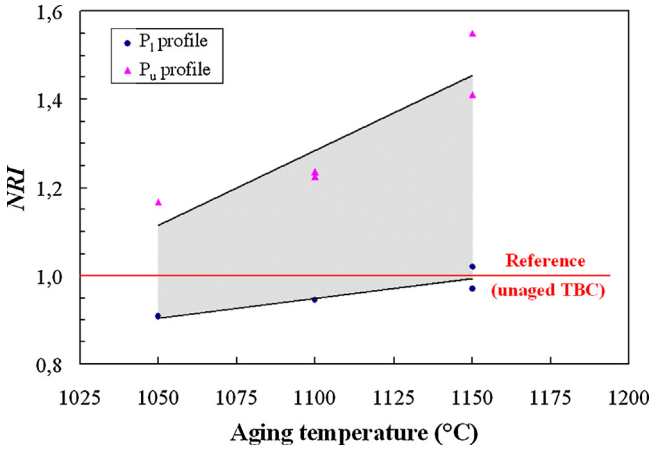


Fig. 17. Evolution of the normalized rumpling index (*NRI*), measured on lower ($P_l$) and upper ($P_u$) profiles of the TGO layer, as a function of the temperature of isothermal aging tests.

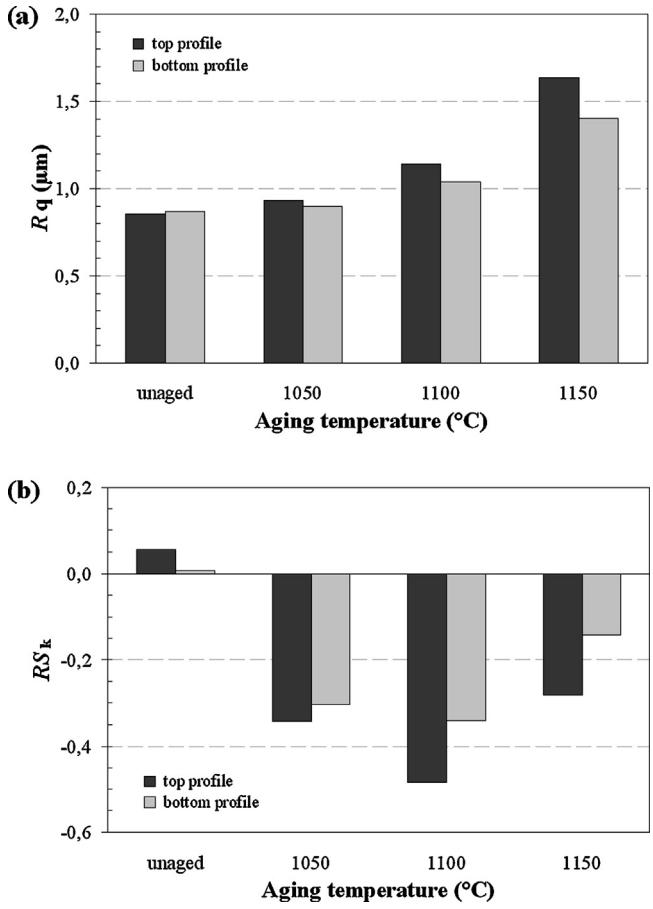


Fig. 18. Evolution versus aging temperature of roughness parameters at the interface between the TGO layer and the ceramic top coat: (a) root-mean-square $R_q$, which indicates that the defect amplitude increases by increasing the temperature; (b) skewness $RS_k$, which expresses the asymmetry of the profile relative to the mean line.

following cyclic exposure at high temperature. This structural change, so-called "rumpling", results from the deformation of the underlying substrate subsequently to the accumulation of oxidation cycles and the associated thermal stress. The deformation may provoke the corrugation of the TGO at the TBC/substrate interface and the propensity of the system to develop rumpling is related to the capability of the deposit, according to its mechanical properties, to avoid or not the establishment of plastic strain under the stress state due to thermal cycling and TGO growth stress. Note that *NRI* is above 1 at the $P_u$ interface, but lower than or close to 1 at the $P_l$ interface (Fig. 17). Consequently, rumpling of thermally aged samples appear to preferentially affect the TBC–TGO interface, which would be more prone to break. This is consistent with observations made by Tolpygo et al.[29] on similar EB-PVD TBC systems investigated under cyclic oxidation at 1150 °C. Rumpling is a consequence of the thermal expansion mismatch between the TGO layer (with a coefficient of thermal expansion $\alpha$ of $8–9\times10^{-6}\,°C^{-1}$) and the upper and lower layers (TBC coating with $\alpha = 11–13\times10^{-6}\,°C^{-1}$ and bond coat with $\alpha = 13–16\times10^{-6}\,°C^{-1}$), leading to alternating compressive/tensile stresses at the interfaces between the different layers. In addition, Fig. 19 indicates that the thickness of the TGO

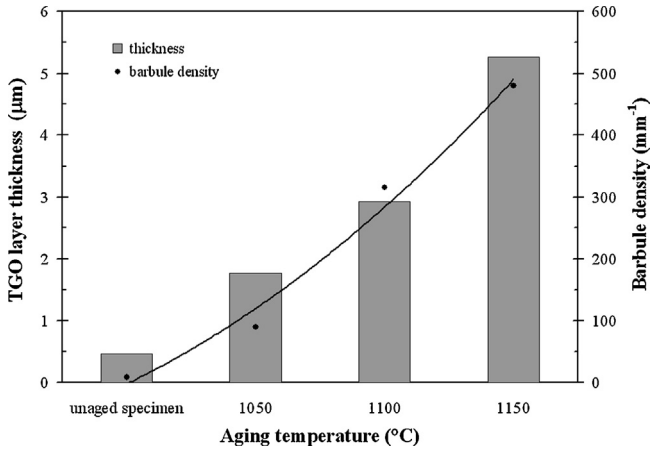


Fig. 19. Evolution of the thickness and barbule density of the TGO layer as a function of the temperature of isothermal aging tests.

Table 6
Apparent toughness $K_{ca}$ measured at the interface between the TBC coating and the substrate by interfacial indentation tests on samples oxidized at various temperatures.

| Oxidation conditions | Critical load $P_c$ (N) | Crack length $a_c$ (µm) | Apparent toughness $K_{ac}$ (MPa $m^{0.5}$) |
|---|---|---|---|
| Unaged | 11.3 | 50.4 | 3.31 |
| 1050 °C–100 h | 2.09 | 14.7 | 2.98 |
| 1100 °C–100 h | 0.85 | 8.5 | 2.57 |
| 1150 °C–100 h | 0.34 | 4.9 | 2.35 |

layer and the "barbule density" also increase as a function of the aging temperature. As illustrated in Fig. 16a, these barbules appear preferentially above the layer median axis. The increasing number of barbules with the oxidation temperature thus reflects the formation of local "protrusions", due to a heterogeneous growth of the TGO layer. This is probably related to the EB-PVD process, which favors a columnar grain growth in the ceramic surface layer and the formation of inter-columnar porosities.

In parallel, the apparent interfacial toughness $K_{ac}$, measured by interfacial indentation tests, drastically decreases upon thermal aging, lowering the adhesion of the TBC system over the substrate (Table 6). This suggests the existence of a relationship between the mechanical strength of the TBC system and the roughness of its interface with the substrate. It must however be emphasized that rumpling is not the unique cause responsible for the failure of the TBC system. In fact, the thickness and chemical composition of the TGO layer, which vary depending on the aging temperature, may also influence the physical and mechanical properties of the coating, and therefore its adhesion to the substrate.[14,29,41]

## 6. Conclusion

The interfacial roughness of oxide layers or of thermal barrier coatings is investigated by image analysis on cross-sectional images. The procedure consists in acquiring a number of contiguous images-fields on a prescribed length, with an appropriate

magnification and resolution selected according to the required observation scale. Image analysis algorithms are developed to extract the profile(s) of the surface or internal layer based on the difference of microstructure. The profiles extracted from each image are saved in an *ASCII* file, assembled, and mathematically processed in order to be calibrated, leveled and filtered. Quantitative parameters are proposed to describe the roughness of the interface profile, like the fractal dimension $L_d/L_p$ relative to the normalized developed length, or conventional roughness parameters (such as $R_a$, $R_z$, $R_q$, ...) calculated according to the surface metrology standards. The method is validated by comparative measurements by stylus profilometry and extended field confocal microscopy, performed on the superficial oxidation layer thermally grown on a composite ceramic sample. The accuracy obtained is satisfactory and the representativeness of results is relevant. Finally, two application cases are exposed to show the potential information provided by this original method. The first one concerns the investigation of the effects of oxidation of a ceramic composite $Si_3N_4$–TiN thermally aged in air at 1150 °C on its mechanical properties. It is shown that the strength of pre-oxidized specimens in bending tests is correlated to the interfacial roughness of the partially oxidized layer. The second case study deals with the thermal aging of thermal barrier coating systems elaborated by EB-PVD process. A relation is highlighted between the ratcheting of the bond coat interface (measured by roughness parameters) and the adhesion of the TBC system on the substrate (measured here by interfacial indentation tests).

Although it is destructive, the characterization technique developed is applicable to any kind of (multi-)layered materials, provided that the layer(s) of interest is (are) distinguishable either by optical or scanning electron microscopy. It provides a quantitative analysis of the interfacial roughness and/or waviness of corrosion layers or surface coatings, difficult to reach by other conventional techniques, with good reproducibility and precision. In addition, it allows to estimate other relevant information such as the thickness of the (sub-)layer(s). Combined with mechanical characterization (such as interfacial indentation tests, flexure tests, laser shock waves, ...), those morphological criteria can help to understand the mechanisms that govern adhesion of coatings deposited by any surface treatment process (such as CVD, PVD, plasma spraying, laser cladding, sol-gel process, etc.). However, note that the approach proposed in the paper does not include full consideration of microstructural details, in particular the density and evolution of interfacial defects and the substrate crystal characteristics (grain size, texture, etc.). Indeed, in order to accurately model the mechanical behavior of multimaterials with a gradient of composition, it would be of course necessary to take into account possible associated long range length scale effects.

## Acknowledgments

The authors gratefully acknowledge Yinghui Liu and Serge Tovar for sample preparation and SEM observations, and Dr. Vanessa Vidal for fruitful discussions.

## References

1. Cook RH, Skelton RP. Environment-dependence of the mechanical properties of metals at high temperature. *Int Mater Rev* 1974;**19**(1):199–222.
2. Molins R, Hochstetter G, Chassaigne JC, Andrieu E. Oxidation effects on the fatigue crack growth behaviour of alloy 718 at high temperature. *Acta Mater* 1997;**45**(2):663–74.
3. Chen TH, Weng KL, Yang JR. The effect of high-temperature exposure on the microstructural stability and toughness property in a 2205 duplex stainless steel. *Mater Sci Eng A* 2002;**338**(1):259–70.
4. Pather R, Mitten WA, Holdway P, Ubhi HS, Wisbey A, Brooks JW. The effect of high temperature exposure on the tensile properties of γ TiAl alloys. *Intermetallics* 2003;**11**(10):1015–27.
5. Deschaux-Beaume F, Cutard T, Fréty N, Levaillant C. Oxidation of $Si_3N_4$–TiN composites in air. *Adv Sci Technol* 1999;**13**:A389–96.
6. Dour G, Lamesle P, Salem M, Le Roux S, Rézaï-Aria F. Oxidation and corrosion effects on thermal fatigue behaviour of hot work tool steel X38CrMoV5 (AISI H11). *Mater Sci Forum* 2008;**595**:789–96.
7. Sobolev VV, Guilemany JM, Nutting J, Miquel JR. Development of substrate-coating adhesion in thermal spraying. *Int Mater Rev* 1997;**42**(3):117–36.
8. Staia MH, Ramos E, Carrasquero A, Roman A, Lesage J, Chicot D, et al. Effect of substrate roughness induced by grit blasting upon adhesion of WX-17% Co thermal sprayed coatings. *Thin Solid Films* 2000;**377–378**:657–64.
9. Wang YY, Li CJ, Ohmori A. Influence of substrate roughness on the bonding mechanisms of high velocity oxy-fuel sprayed coatings. *Thin Solid Films* 2005;**485**(1):141–7.
10. Amada S, Yamada H. Introduction of fractal dimension to adhesive strength evaluation of plasma-sprayed coatings. *Surf Coat Technol* 1996;**78**(1):50–5.
11. Habig KH. Wear behaviour of surface coatings on steels. *Tribol Int* 1989;**22**(2):65–73.
12. Evans AG, Mumm DR, Hutchinson JW, Meier GH, Pettit FS. Mechanisms controlling the durability of thermal barrier coatings. *Prog Mater Sci* 2001;**46**(5):505–53.
13. Schulz U, Leyens C, Fritscher K, Peters M, Saruhan-Brings B, Lavigne O, et al. Some recent trends in research and technology of advanced thermal barrier coatings. *Aerosp Sci Technol* 2003;**7**(1):73–80.
14. Tolpygo VK, Clarke DR, Murphy KS. Evaluation of interface degradation during cyclic oxidation of EB-PVD thermal barrier coatings and correlation with TGO luminescence. *Surf Coat Technol* 2004;**188**:62–70.
15. Zhang D, Gong S, Xu H, Wu Z. Effect of bond coat surface roughness on the thermal cyclic behavior of thermal barrier coatings. *Surf Coat Technol* 2006;**201**(3):649–53.
16. Freborg AM, Ferguson BL, Brindley WJ, Petrus GJ. Modeling oxidation induced stresses in thermal barrier coatings. *Mater Sci Eng A* 1998;**245**(2):182–90.
17. Pindera MJ, Aboudi J, Arnold SM. The effect of interface roughness and oxide film thickness on the inelastic response of thermal barrier coatings to thermal cycling. *Mater Sci Eng A* 2000;**284**(1):158–75.
18. Ahrens M, Vaßen R, Stöver D. Stress distributions in plasma-sprayed thermal barrier coatings as a function of interface roughness and oxide scale thickness. *Surf Coat Technol* 2002;**161**(1):26–35.
19. Balint DS, Hutchinson JW. An analytical model of rumpling in thermal barrier coatings. *J Mech Phys Solids* 2005;**53**(4):949–73.
20. Whitehouse DJ. *Handbook of surface and nanometrology*. 2nd ed. Boca Raton: CRC Press; 2011.
21. Whitehouse DJ. Comparison between stylus and optical methods for measuring surfaces. *CIRP Ann Manuf Technol* 1988;**37**(2):649–53.
22. Poon CY, Bhushan B. Comparison of surface roughness measurements by stylus profiler, AFM and non-contact optical profiler. *Wear* 1995;**190**(1):76–88.
23. Mandelbrot BB. *The fractal geometry of nature. Revised and enlarged ed*. New York: WH Freeman & Co.; 1983.
24. Voss RF. Characterization and measurement of random fractals. *Phys Scr* 1986;**T13**:27–32.
25. Berry M, Hannay J. Topography of random surfaces. *Nature* 1978;**273**:573.
26. Mandelbrot BB, Passoja DE, Paullay AJ. Fractal character of fracture surfaces of metals. *Nature* 1984;**308**:721–2.

27. Mecholsky JJ, Passoja DE, Feinberg-Ringer KS. Quantitative analysis of brittle fracture surfaces using fractal geometry. *J Am Ceram Soc* 1989;**72**(1):60–5.
28. Trefilov VI, Kartuzov VV, Minakov NV. Fractal dimension of fracture surfaces. *Met Sci Heat Treat* 2001;**43**(3–4):95–8.
29. Tolpygo VK, Clarke DR, Murphy KS. On the rumpling mechanism in nickel-aluminide coatings: Part II: characterization of surface undulations and bond coat swelling. *Acta Mater* 2004;**52**(17):5129–41.
30. Serra J. *Image analysis and mathematical morphology*, Vol. 2. London: Academic Press; 1982.
31. International Standard ISO 4288. *Geometrical Product Specifications (GPS) – surface texture: profile method – rules and procedures for the assessment of surface texture*. Geneva: International Organization for Standardization; 1996.
32. Mummery L. *Surface texture analysis—the handbook*. 2nd ed. Muhlhausen (Germany): Hommelwerke GmbH; 1992.
33. Gurau L, Mansfield-Williams H, Irle M. Filtering the roughness of a sanded wood surface. *Holz als Roh-und Werkstoff* 2006;**64**(5):363–71.
34. Raja J, Muralikrishnan B, Fu S. Recent advances in separation of roughness, waviness and form. *Precis Eng* 2002;**26**(2):222–35.
35. International Standard ISO 11562. *Geometrical Product Specifications (GPS) – surface texture: profile method – metrological characteristics of phase correct filters*. Geneva: International Organization for Standardization; 1996.
36. International Standard ISO 4287. *Geometrical Product Specifications (GPS) – surface texture: profile method – terms, definitions and surface texture parameters*. Geneva: International Organization for Standardization; 1997.
37. O'Donnell KA. Effects of finite stylus width in surface contact profilometry. *Appl Opt* 1993;**32**(25):4922–8.
38. Deschaux-Beaume F, Fréty N, Cutard T, Colin C. Oxidation modeling of a $Si_3N_4$–TiN ceramic: microstructure and kinetic laws. *Ceram Int* 2007;**33**(7):1331–9.
39. Wang F, Zheng XL, Lu MX. Notch strength of ceramics and statistical analysis. *Eng Fract Mech* 1995;**52**(5):917–21.
40. Sniezewski J, Vidal V, Lours P, Le Maoult Y. Thermal barrier coatings adherence and spallation: interfacial indentation resistance and cyclic oxidation behaviour under thermal gradient. *Surf Coat Technol* 2009;**204**(6):807–11.
41. Sniezewski J, Le Maoult Y, Lours P. Oxidation and spallation of FeCrAl alloys and thermal barrier coatings: in situ investigation under controlled temperature gradient. *Mater High Temp* 2010;**27**(2):101–8.